Inorganic Chemistry

Article

pubs.acs.org/IC

Nanocellulose-Assisted Formation of Porous Hematite Nanostructures

Alesja Ivanova,[†] Ksenia Fominykh,[†] Dina Fattakhova-Rohlfing, Patrick Zeller, Markus Döblinger, and Thomas Bein*

Department of Chemistry and Center for NanoScience (CeNS), University of Munich (LMU), Butenandtstrasse 5-13 (E), 81377 Munich, Germany

Supporting Information

ABSTRACT: We report the formation of porous iron oxide (hematite) nanostructures via sol–gel transformations of molecular precursors in the confined space of self-organized nanocrystalline cellulose (NCC) used as a shape-persistent template. The obtained structures are highly porous α-Fe_2O_3 (hematite) morphologies with a well-defined anisotropic porosity. The character of the porous nanostructure depends on the iron salt used as the precursor and the heat treatment. Moreover, a postsynthetic hydrothermal treatment of the NCC/iron salt composites strongly affects the crystal growth as well as the porous nanomorphology of the obtained hematite scaffolds. We demonstrate that the hydrothermal treatment alters the crystallization mechanism of the molecular iron precursors, which proceeds via the formation of anisotropic iron oxyhydroxide species. The nanocellulose templating technique established here enables the straightforward fabrication of a variety of mesoporous crystalline iron oxide scaffolds with defined porous structure and is particularly attractive for the processing of porous hematite films on different substrates.

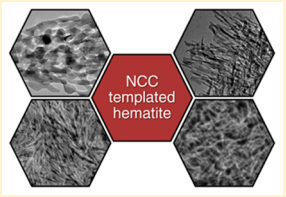

INTRODUCTION

The combination of semiconducting properties with low cost, abundance, and chemical stability makes iron oxides attractive materials for various energy conversion and storage applications. Among numerous iron oxide compounds, α-Fe_2O_3 (hematite) is the most studied material whose applications span from electrochemical energy storage and photoelectrochemical water splitting to photocatalytic degradation of air and water pollutants and gas sensing.[1−3] The performance of hematite in these applications critically depends upon mass transfer to the active surface sites, charge transfer at the interface, and charge and/or ion transport in the bulk. These processes are controlled to a large degree by the nanomorphology of iron oxide because of the role of interface-related processes caused by the large surface area, as well as the impact of the diminishing dimensions on its charge-carrier and ion-transport behavior. Because of the interest in nanostructured iron oxide, several strategies have already been developed for the fabrication of nanomorphologies with optimized properties.[4−6] Still, a major synthetic challenge is control over the structure on different length scales, from the organization of atoms in the crystalline structure to the macroscopic morphology, which strongly influences the performance of hematite in different applications.

Templated approaches based on sol–gel transformations of molecular precursors can provide a high level of control over the porous nanostructure by using objects with a well-defined shape and 3D organization to guide evolution of the structure and morphology. Mesoporous nanocrystalline iron oxide thin films with high surface area have been prepared by so-called soft-templating methods using supramolecular aggregates (micelles) of amphiphilic molecules.[7,8] The practical benefits of soft templating include the straightforward formation of periodic porous structures based on the self-assembly processes and the facile subsequent removal of the organic templates by thermal decomposition. However, the critical step in these transformations is crystallization of the inorganic scaffold, which often leads to collapse of the porous morphology due to uncontrolled crystal growth at elevated temperatures and requires a careful selection of the amphiphilic molecules and/or the processing conditions. Alternatively, hard-templating routes are advantageous regarding the formation of highly crystalline transition-metal oxide morphologies with well-defined porosity.[9−11] Thermally stable and robust templates such as porous silica or alumina have been demonstrated to sustain the crystallization of porous transition-metal oxides, but these methods are less suitable for the processing of porous coatings on different substrates because of the difficulties associated with the removal of the template under demanding conditions.

Nanocrystalline cellulose (NCC) extracted from natural cellulose sources[12,13] is a promising biogenic template for the generation of porosity in inorganic oxides. Cellulose nanocrystals having anisotropic rodlike shape show a remarkable ability to self-organize and to form chiral nematic liquid-crystalline phases.[14,15] Owing to the rigidity and thermal stability of the cellulose nanocrystals, the NCC-based

Special Issue: To Honor the Memory of Prof. John D. Corbett

Received: October 7, 2014
Published: December 30, 2014

DOI: 10.1021/ic502446f
Inorg. Chem. 2015, 54, 1129−1135

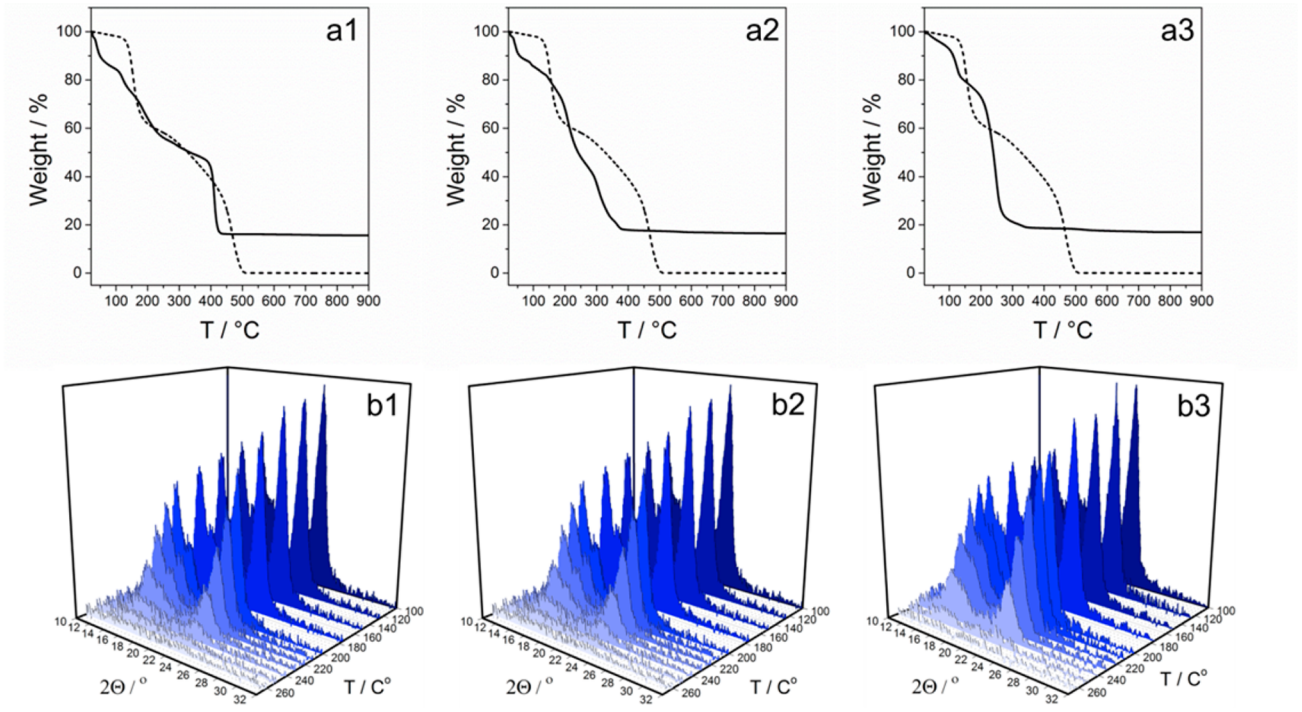

Figure 1. Degradation of NCC/iron oxide precursor composites containing different iron salts: $FeCl_3 \cdot 6H_2O$ (a1 and b1), $FeCl_2 \cdot 4H_2O$ (a2 and b2), and $Fe(NO_3)_3 \cdot 9H_2O$ (a3 and b3). Top row (a1–a3): TGA revealing mass loss of iron oxide precursor/NCC composites (black lines) compared to pristine NCC (dashed lines). The composites were dried at 35 °C prior to analysis and heated with a ramp of 2 °C/min. Bottom row (b1–b3): In situ XRD patterns obtained upon gradual heating of 1 μm iron oxide precursor/NCC composite films coated on silicon wafers.

composites can sustain relatively high temperatures and provide fully crystalline metal oxide scaffolds with well-defined mesostructure, therefore combining the advantages of soft templating and shape-persistent hard templates.

Recent studies on the preparation of nanoscale iron oxide aided by cellulose have focused mainly on composite materials.[16−24] In these publications, cellulose of different origins acts as a supporting matrix for the formation of iron oxide and as a filler for the homogeneous distribution of presynthesized crystalline nanospecies. Other biomaterials have been shown to assist in the nanofabrication of iron oxide, such as silk,[25] chitosan,[26−28] chitin,[29] proteins,[30] yeast cells,[31] and butterfly wings.[32] A few publications describing the fabrication of porous hematite morphologies aided by sacrificial cellulose templating[33−35] deal only with macroscopic cellulose-based objects such as wood, filter paper, or fibers fabricated from regenerated cellulose. On the contrary, in our study we employ distinct nanosized cellulose species for the synthesis of porous hematite nanostructures. Recently, we have established the high potential of cellulose nanocrystals in the fabrication of porous titania thin films.[36] Herein we explore the suitability of this promising approach for the synthesis of iron oxide films. We show for the first time the direct formation of porous hematite thin films on different substrates by a nanocellulose-assisted templating method. We demonstrate several strategies to alter the scaffold morphology. In particular, we investigate the effect of iron oxide precursors and the calcination temperature on the film porosity and crystallinity. Furtheremore, we reveal a striking effect of postsynthetic treatments on the crystallization of iron oxide in the nanocellulose matrix.

RESULTS AND DISCUSSION

For the fabrication of mesoporous iron oxide, aqueous dispersions of NCC were mixed with different iron salts acting as iron oxide precursors in the sol–gel process. As such, we used hydrates of iron(III) nitrate [$Fe(NO_3)_3 \cdot 9H_2O$], iron(III) chloride ($FeCl_3 \cdot 6H_2O$), and iron(II) chloride ($FeCl_2 \cdot 4H_2O$), which are perfectly soluble in the NCC dispersions without changes in their colloidal stability. Iron(III) salts color the opaque cellulose suspensions yellow, whereas the iron(II) chloride solution remains white. After dissolution, the precursor mixtures were processed to powders or films by drop-casting on Teflon surfaces or spin-coating on different substrates (typically silicon wafers or fluorine-doped tin oxide, FTO), respectively. After drying, the composites were calcined in air at temperatures ranging from 300 to 600 °C to remove cellulose under formation of mesoporous iron oxide scaffolds.

Thermogravimetric analysis (TGA) of pure NCC reveals that it dehydrates in several subsequent steps in the temperature range from 200 to 500 °C[37,38] and that it is completely decomposed at 500 °C. The addition of iron salts leads to a decrease in the decomposition temperature, which depends on the type of precursor, as demonstrated in Figure 1a1–a3.

According to the TGA measurements, the lowest decomposition temperature of ca. 290 °C was observed for the NCC/$Fe(NO_3)_3 \cdot 9H_2O$ composite, which could be attributed to the oxidative character of the nitrate ions. The addition of iron(III) chloride leads to a rather small decrease in the decomposition temperature to ca. 450 °C, while in the iron(II) chloride containing composites, NCC is combusted at about 400 °C.

In order to investigate the degradation behavior of the nanocellulose in thin films, we performed in situ X-ray diffraction (XRD) heating experiments on 1-μm-thick composite films coated on silicon wafers. Parts b1–b3 of

DOI: 10.1021/ic502446f
Inorg. Chem. 2015, 54, 1129–1135

Figure 1 show a gradual reduction of the signals characteristic for native cellulose upon a temperature increase [the NCC signal assignment is shown in Figure S1 in the Supporting Information (SI)]. Although the XRD results indicate complete degradation of crystalline cellulose at 250 °C, the optical appearance of the films calcined at this temperature implies the presence of template residues, as follows from the black coloring of the film (Figure S2d in the SI), which is consistent with TGA revealing an incomplete decomposition of cellulose at 250 °C (Figure 1).

The degradation studies demonstrate that calcination of composite films at 300−600 °C should be sufficient to remove NCC with the associated liberation of open pores. This is confirmed with scanning electron microscopy (SEM) images of the NCC-templated films, which demonstrate the formation of elongated slitlike pores characteristic for NCC-derived porous scaffolds, closely replicating the shape of the initial NCC (Figure 2). The mesoporous morphology obtained after calcination of the dried coatings is practically not influenced by the choice of iron precursors (SEM images in Figures 2 and S3 in the SI). The porous texture changes only slightly with increasing calcination temperature from 300 to 500 °C, corresponding to the stability range of NCC. However, calcination at 600 °C leads to significant crystal growth with the formation of wormlike disordered porous layers typically observed for different solution-processed hematite films (Figure 2d).

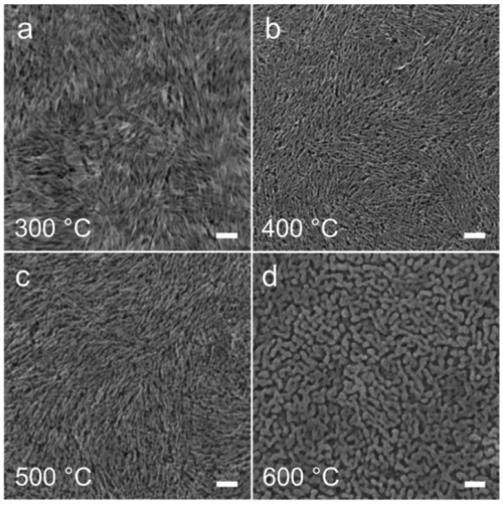

Figure 2. SEM top-view images revealing the effect of the calcination temperature on the morphology of NCC-templated α-Fe_2O_3 thin films. The films were coated on silicon wafers from solutions containing NCC and $FeCl_3 \cdot 6H_2O$ and calcined at (a) 300, (b) 400, (c) 500, and (d) 600 °C. The scale bars correspond to 100 nm.

Analysis by transmission electron microscopy (TEM) confirms the increase of the feature sizes for the NCC-templated film calcined at 600 °C, compared to the one heated at 500 °C. The samples exhibit a highly porous structure and a crystalline morphology, as can be seen in the high-resolution and selected-area electron diffraction (SAED) images (Figures 3 and S4 in the SI). The determined *d*-spacing values are typical of hematite and agree very well with previous studies.[39]

In order to study the temperature-induced formation of crystalline iron oxide in the presence of nanocellulose, we performed XRD measurements on cast free-standing composites. Figures 4 and S5a in the SI reveal formation of the α-Fe_2O_3 phase for all precursors at temperatures higher than 300 °C.

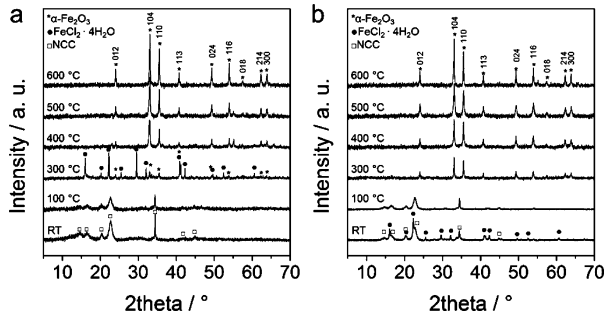

Figure 4. XRD patterns of NCC-templated iron oxide free-standing films cast from $FeCl_3 \cdot 6H_2O$ (a) and $FeCl_2 \cdot 4H_2O$ (b) precursor solutions. The composites were dried overnight [assigned as room temperature (RT)] and then either heated at 100 °C overnight or calcined at 300−600 °C for 30 min. The assigned signals correspond to native cellulose (ICDD pattern C00-003-0289; □), iron(II) chloride tetrahydrate (ICDD pattern 00-016-0123; ●), and hematite (ICDD pattern 00-003-0289; *).

Surprisingly, heating of the iron(III) chloride/NCC composite at 300 °C initially leads to the formation of hematite and iron(II) chloride, which could be due to a reaction of iron(III) chloride with NCC degradation products.

To modify the crystallization of hematite, the dried composite films were post-treated at 100 °C in high humidity,

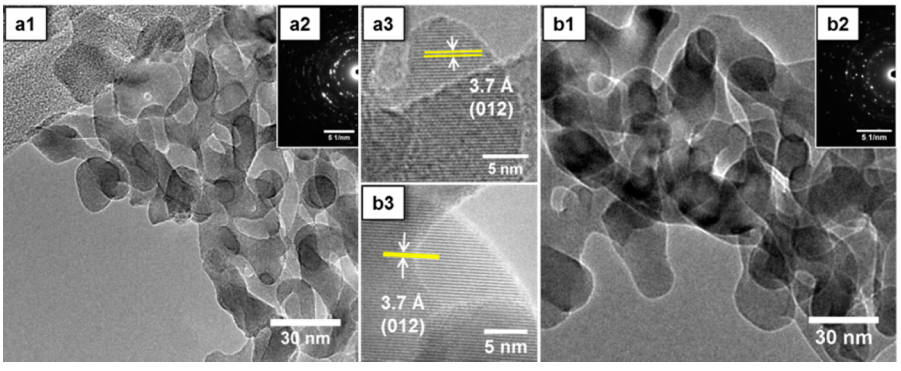

Figure 3. TEM images (a1, a3, b1, and b3) and SAED patterns (a2 and b2) of NCC-templated iron oxide thin films prepared from $FeCl_2 \cdot 4H_2O$ precursor solutions and calcined at (a) 500 and (b) 600 °C.

DOI: 10.1021/ic502446f
Inorg. Chem. 2015, 54, 1129−1135

also known as delayed humidity treatment (DHT). This procedure can be considered as a hydrothermal treatment of the iron salts in the confined space of the prearranged NCC template rods. The XRD analysis reveals formation of a crystalline inorganic phase corresponding to crystalline iron oxyhydroxide (β-FeOOH, akaganeite) after DHT (Figure 5).

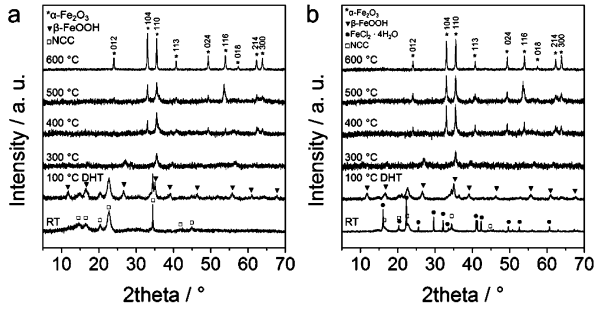

Figure 5. XRD patterns of NCC-templated iron oxide free-standing films cast from $FeCl_3 \cdot 6H_2O$ (a) and $FeCl_2 \cdot 4H_2O$ (b) precursor solutions. The dried composites (assigned as RT) were postsynthetically treated overnight at 100 °C in high humidity (set to 85% relative humidity at RT) and then calcined at 300–600 °C for 30 min. The assigned signals correspond to native cellulose (ICDD pattern 00-003-0289; □), iron(II) chloride tetrahydrate (ICDD pattern 00-016-0123; ●), akaganeite (ICDD pattern 00-034-1266; ▼), and hematite (ICDD pattern 00-033-0664; *).

We note that heating at 100 °C without hydrothermal treatment does not lead to formation of a crystalline phase (Figure 4). Our results imply that without the postsynthetic humidity treatment either amorphous iron oxide directly transforms to the crystalline hematite or the intermediate phase is not stable and rapidly converts to the hematite. Moreover, we found that DHT facilitates crystallization of the oxyhydroxide species in the composite based on both iron(II) and iron(III) chlorides, although this is not the case for the nitrate hydrate precursor treated at the same conditions (Figure S5b in the SI). It has been previously shown that at certain conditions hydrolysis of iron chlorides proceeds through the formation of α,β-FeOOH oxyhydroxide phases prior to full conversion to α-Fe_2O_3.[40−43]

To elucidate the effect of the postsynthetic treatment, the iron chloride/NCC composites were dried at different conditions and studied by X-ray photoelectron spectroscopy (XPS). Figures 6 and S6 in the SI show evolution of the peaks arising from oxygen, chlorine, iron, and carbon depending on the film drying conditions.

The most significant changes were observed for the oxygen and chlorine peaks shown in Figure 6. The oxygen peak shifts toward lower binding energies (Figure 6a1) with increasing temperature from RT to 300 °C, indicating the release of H_2O, degradation of cellulose, and formation of iron species containing OH^- and O^{2-} (the fitting is shown in Figure S6a3 in the SI).[44,45] In addition, chloride completely degrades at 300 °C (Figure 6a2). Interestingly, heating at 100 °C under hydrothermal conditions (DHT) leads to a significant decrease in the chloride contents, whereas after heating in air at the same temperature, the chloride is well-preserved (the black and red lines in Figure 6a2, respectively). This behavior indicates a higher degree of hydrolysis of iron chlorides because of the presence of water vapor, which is also consistent with the shape of the oxygen spectra recorded for the DHT samples. The black

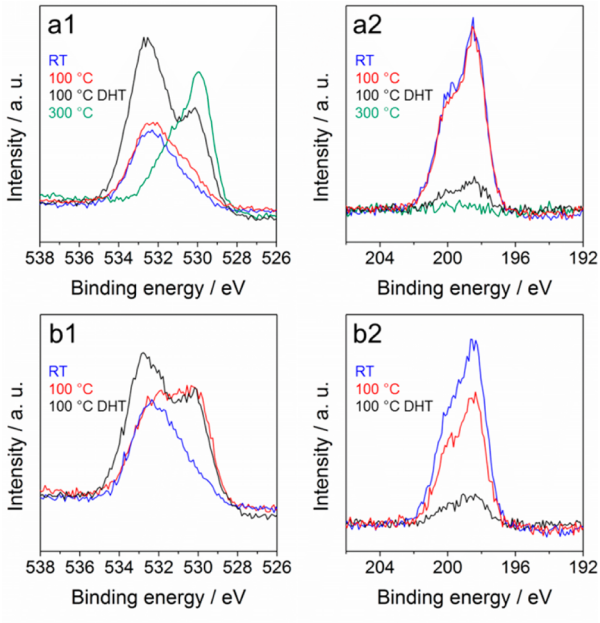

Figure 6. XPS spectra of O 1s (a1 and b1) and Cl 2p (a2 and b2) measured on iron chloride/NCC composite films coated on silicon wafers, resulting from $FeCl_3 \cdot 6H_2O$ (a1 and a2) and $FeCl_2 \cdot 4H_2O$ (b1 and b2) precursors and dried at different conditions: at RT, at 100 °C in humid air (assigned as 100 °C DHT), and at 100 and 300 °C in ambient humidity conditions.

spectra in Figure 6a1,b1 demonstrate a doublet with a pronounced signal corresponding to water and cellulose at 532.5 eV and a less intense peak at lower binding energies (530.1 eV) related to O^{2-} in iron oxide. The spectra point to hydration of cellulose and formation of oxygen bridges in the inorganic part of the composites. We found that the iron(II) chloride composite loses some chlorine already after ambient heating at 100 °C and contains iron oxide O^{2-} species, which was not the case for the iron(III) chloride sample (red spectra in parts b2 and a2 in Figure 6, respectively). In conclusion, XPS analysis points to accelerated hydrolysis and nucleation of the crystalline phase due to DHT. Additionally, the increase of the signal at about 533 eV implies high contents of water in the samples, which may reduce shrinkage of the cellulose species due to swelling at high relative humidity.[46]

Notably, we found that induced crystallization of iron oxyhydroxide during the postsynthetic treatment significantly affects the film morphologies after calcination, as demonstrated in Figures 7 and S7 in the SI.

DHT results in an anisotropic geometry of iron oxide species, which is especially pronounced for the films calcined at low temperatures of 300–400 °C (Figure 7a,b). However, thermal treatment at higher temperatures leads to recrystallization of the nanorods to form intergrown roundly shaped species (Figure 7d). A more detailed investigation of the DHT effect on crystal formation is shown in Figure 8.

TEM analysis in Figure 8 reveals a similar trend in the crystallization pathway for both $FeCl_3 \cdot 6H_2O$ and $FeCl_2 \cdot 4H_2O$ precursors. Calcination at the moderate temperature of 400 °C leads to the formation of crystalline species showing a pronounced anisotropic shape, with a length of around 55 nm and a width of around 5 nm (Figure 8a1-1). Additionally, the crystals obtained with $FeCl_2 \cdot 4H_2O$ (Figure 8b1-1) show a porous structure, which can be attributed to dehydration during

DOI: 10.1021/ic502446f
Inorg. Chem. 2015, 54, 1129−1135

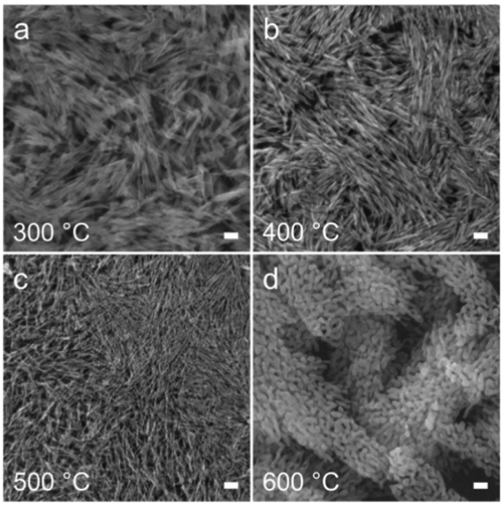

Figure 7. SEM top-view images revealing the effect of the calcination temperature on the morphology of the NCC-templated α-Fe_2O_3 thin films postsynthetically treated in humid air at 100 °C prior to calcination at (a) 300, (b) 400, (c) 500, and (d) 600 °C. The films were coated on silicon wafers from solutions containing NCC and $FeCl_2 \cdot 6H_2O$. The scale bars correspond to 100 nm.

thermal conversion from β-FeOOH to α-Fe_2O_3.[47] At 500 °C, the elongated shape of the features is still present, although it is clearly visible that the particles start to recrystallize, forming a polycrystalline network with the formation of additional more spherically shaped species. The length of the rods is around 30 nm, while the rod width remains approximately 5 nm. The lattice fringes of the elongated crystals correspond to (104) hematite planes, as can be seen in the high-resolution TEM images in Figure 8. At 600 °C, the recrystallization step is more pronounced, and the species have a nearly spherical geometry with a size of ca. 25 nm length and 20 nm width. Accordingly, the aspect ratio of the rods decreases from about 12 to 1.3 with increasing calcination temperature.

Iron(III) nitrate does not undergo oxyhydroxide-to-hematite transformation; therefore, DHT does not have a pronounced effect on the NCC-templated hematite morphology (Figure S7 in the SI). We note that all obtained NCC-templated hematite scaffolds exhibit a rather similar specific surface area of about 65 m^2/g (Figure S8 in the SI).

CONCLUSIONS

We have established a facile method for the synthesis of crystalline and highly porous iron oxide thin films with various nanomorphologies by employing the biogenic template nanocellulose. Different iron salts, namely, $FeCl_3 \cdot 6H_2O$, $FeCl_2 \cdot 4H_2O$, and $Fe(NO_3)_3 \cdot 9H_2O$, can be successfully employed for the NCC-assisted synthesis. The nature of the calcination procedure of the NCC/iron oxide precursor composites has a strong influence on the morphology of the porous hematite films.

Furthermore, we show that a postsynthetic humidity treatment at elevated temperature drastically affects the morphology of the porous scaffolds prepared from $FeCl_3 \cdot 6H_2O$ and $FeCl_2 \cdot 4H_2O$. Upon exposure to the humidity treatment at 100 °C, the crystallization of hematite proceeds through the formation of iron oxyhydroxide (β-FeOOH)

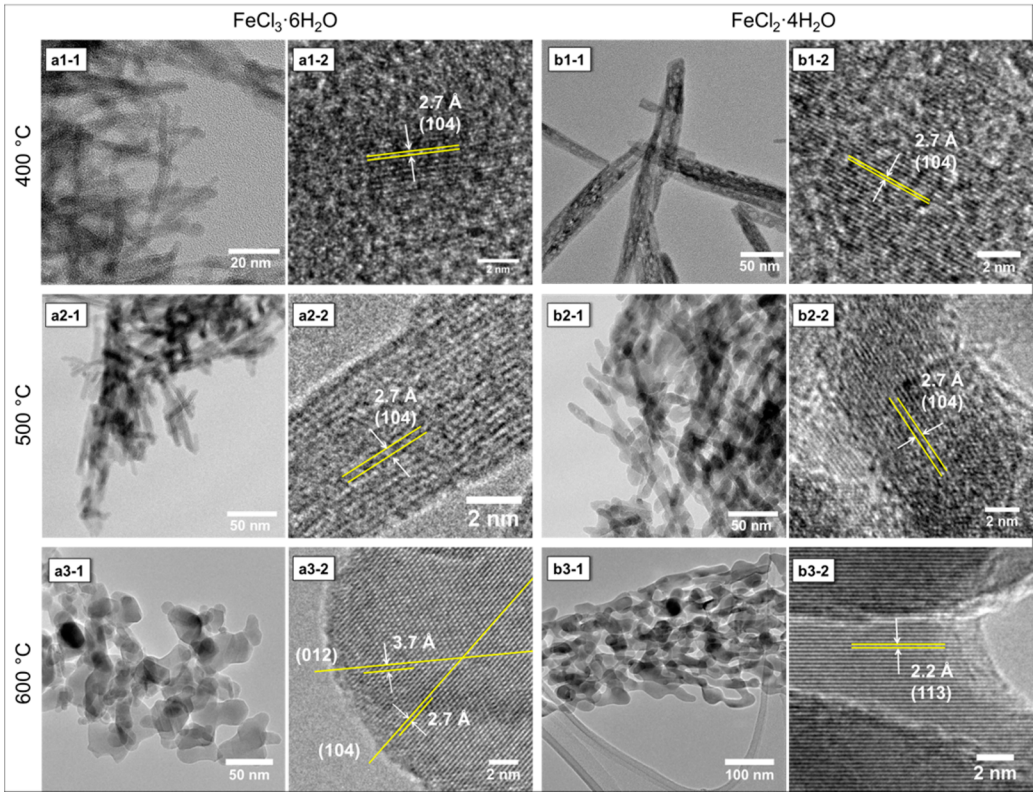

Figure 8. TEM images at low and high magnifications of iron oxide thin films prepared from iron chloride/NCC solutions coated on silicon wafer, obtained from $FeCl_3 \cdot 6H_2O$ (a) and $FeCl_2 \cdot 4H_2O$ (b) precursors. The composites were exposed to humidity treatment at 100 °C and subsequently calcined at (a1 and b1) 400, (a2 and b2) 500, and (a3 and b3) 600 °C.

DOI: 10.1021/ic502446f
Inorg. Chem. 2015, 54, 1129−1135

species of highly anisotropic shape. Because of the shape persistence of cellulose nanocrystals, the film homogeneity and porosity are well preserved despite the complex behavior of hematite crystallization. We show that a great variety of iron oxide networks can be achieved and the morphology of the films can be tuned by facile nanocellulose templating. The above synthesis approach is particularly advantageous for the fabrication of homogeneous porous coatings of iron oxide on different types of substrates.

EXPERIMENTAL SECTION

Extraction of Cellulose Nanocrystals. Nanocrystalline cellulose (NCC) was extracted from cotton linters CP20 (Peter Temming AG) by hydrolysis in sulfuric acid.[48] The cotton fibers were washed with water and dried at 60 °C. Then 64% H_2SO_4 was added to the cotton fibers at a ratio of 1 mL of acid to 8.75 g of cellulose. The mixture was kept at RT for 25 min. Then it was heated at 55 °C for 45 min under vigorous stirring until large cellulose aggregates dissolved. Afterward, the suspension was 10-fold diluted with deionized water and stored overnight. The upper liquid phase was decanted, and the NCC-rich lower phase was washed three times with water via repeated centrifugation at 47808 *g* relative centrifugal force (RFC) for 15 min. The last centrifugation step was performed at 70 *g* RFC for 10 min in order to sediment cellulose aggregates and to collect the suspension of finely dispersed NCC. Finally, the suspension was concentrated in a rotary evaporator to 8.15 wt % at pH 2.55.

Preparation of Precursor Solutions. A total of 1.229 g of the above 8.15 wt % dispersion of cellulose crystals was added to 0.37 mmol of iron salt corresponding to 0.100, 0.0736, and 0.1495 g of $FeCl_3{\cdot}6H_2O$, $FeCl_2{\cdot}4H_2O$, and $Fe(NO_3)_3{\cdot}9H_2O$ salts, respectively. The viscous mixture was vigorously stirred for about 2 min. Then 3.6 g of water was added in order to dilute the cellulose suspension and to dissolve the iron precursor. The precursor solutions contained concentrations of 0.076 M iron and 2 wt % NCC. The solutions were stirred for 2 h prior to film coating.

Film Fabrication. Free-standing films were cast from precursor solutions on a Teflon surface (5 g of a precursor solution on a 6 × 6 cm^2 area) and dried at 35 °C overnight prior to calcination. After calcination, pulverized cast films were analyzed by using XRD, nitrogen sorption measurements, and TGA.

Thin films were deposited on a 1.5 × 2.0 cm^2 silicon wafer or on 1.5 × 2.5 cm^2 FTO glass by spin coating a 100 μL precursor solution at 1500 rpm for 25 s followed by drying for 10 s with a heat gun set at 100 °C. The spin-coating and drying cycles were repeated seven times to achieve ca. 1 μm film thickness of the composites for the XRD degradation experiments and for XPS analysis. For SEM imaging, two layers were coated on silicon wafers.

For DHT, the free-standing films or films coated on substrates were placed into a 2 L desiccator containing 80 mL of KCl-saturated aqueous solution resulting in 85% relative humidity at RT and kept in an oven at 100 °C overnight prior to calcination.

The free-standing films and thin films were heat-treated at 100 °C overnight, 300 °C for 30 min, 400 °C for 30 min, and 600 °C for 30 min with a heating ramp of 3 °C/min. Calcination at 500 °C was performed by using a 2 °C/min ramp with 2 h continuous heating steps at 100 and 360 °C and a final step at 500 °C for 30 min.

Characterization. TGA of the samples was performed on a Netzsch STA 440 C TG/DSC instrument (heating rate of 2 °C/min in a stream of synthetic air of about 25 mL/min).

XRD analysis of the free-standing films was performed on a STOE powder diffractometer in transmission geometry (Cu Kα_1, λ = 1.5406 Å) equipped with a position-sensitive Mythen-1K detector. XRD patterns were collected in a 2θ range from 5° to 70° with a step of 1° and a fixed counting time of 45 s/step. In situ XRD heating measurements of the films on silicon substrates were carried out in reflection mode (Bragg–Brentano) using a Bruker D8 Discover with nickel-filtered Cu Kα radiation and a position-sensitive detector (LynxEye). The instrument was equipped with a heating stage operated by an Anton Paar TCU 200 temperature control unit. The films were heated with a ramp of 1 °C/s and 10 min of continuous heating at the set temperatures.

SEM images were obtained with a Jeol JSM-6500F scanning electron microscope equipped with a field-emission gun operated at 5 kV. The films were prepared on silicon substrates and glued onto a sample holder with silver lacquer.

TEM analysis was performed with thin films removed from the substrate and deposited on a carbon-coated copper grid. Analysis was carried out on a FEI Titan 80-300 (S)TEM equipped with a field-emission gun operated at 300 kV.

XPS analysis was performed with a VSW TA10 X-ray source, providing nonmonochromated Mg Kα radiation, and a VSW HA100 hemispherical analyzer. The samples were cleaned before measurement by 15 min of Ar^+ sputtering (1 kV and ~7 μA). Peak shifts due to charging of the sample were corrected by setting the Cl $2p_{3/2}$ peak to 198.4 eV. The recorded elemental peaks were fitted with a Doniach–Sunjic line shape convoluted with a Gaussian and linear background subtraction.[49]

The nitrogen sorption isotherms were obtained at −196 °C using a Quantachrome Autosorb-1. The specific surface area was determined with the Brunauer–Emmett–Teller method at p/p_0 = 0.05–0.2.

ASSOCIATED CONTENT

Supporting Information

XRD patterns of NCC and iron oxides, photographs of free-standing and thin films, electron micrographs of hematite thin films, XPS spectra of NCC/iron chloride films, and nitrogen sorption isotherms of NCC-templated hematite. This material is available free of charge via the Internet at http://pubs.acs.org.

AUTHOR INFORMATION

Corresponding Author

*E-mail: bein@lmu.de.

Author Contributions

†These authors contributed equally to this work.

Notes

The authors declare no competing financial interest.

ACKNOWLEDGMENTS

The authors are grateful to the German Research Foundation (DFG; Grants FA 839/3-1 and SPP 1613), the NIM cluster (DFG), the research networks "Solar Technologies Go Hybrid" and UMWELTnanoTECH (State of Bavaria), the Center for NanoScience (CeNS), and the German Academic Exchange Service (DAAD) for financial support. The authors acknowledge Dr. Steffen Schmidt and Alexander Müller for TEM measurements. The authors thank Tina Reuther for the nitrogen sorption measurements and Prof. Peter Klüfers (LMU München) for providing cotton linters.

REFERENCES

(1) Sivula, K.; Le Formal, F.; Grätzel, M. *ChemSusChem* **2011**, *4*, 432–449.

(2) Wu, C.; Yin, P.; Zhu, X.; OuYang, C.; Xie, Y. *J. Phys. Chem. B* **2006**, *110*, 17806–17812.

(3) Chen, J.; Xu, L.; Li, W.; Gou, X. *Adv. Mater.* **2005**, *17*, 582–586.

(4) Sivula, K.; Zboril, R.; Le Formal, F.; Robert, R.; Weidenkaff, A.; Tucek, J.; Frydrych, J.; Grätzel, M. *J. Am. Chem. Soc.* **2010**, *132*, 7436–7444.

(5) Srivastava, D. N.; Perkas, N.; Gedanken, A.; Felner, I. *J. Phys. Chem. B* **2002**, *106*, 1878–1883.

(6) Mitra, A.; Vázquez-Vázquez, C.; López-Quintela, M. A.; Paul, B. K.; Bhaumik, A. *Microporous Mesoporous Mater.* **2010**, *131*, 373–377.

DOI: 10.1021/ic502446f
Inorg. Chem. 2015, 54, 1129–1135

(7) Brezesinski, T.; Groenewolt, M.; Antonietti, M.; Smarsly, B. *Angew. Chem., Int. Ed.* **2006**, *45*, 781−784.
(8) Brezesinski, K.; Haetge, J.; Wang, J.; Mascotto, S.; Reitz, C.; Rein, A.; Tolbert, S. H.; Perlich, J.; Dunn, B.; Brezesinski, T. *Small* **2011**, *7*, 407−414.
(9) Zhang, R.; Dai, H.; Du, Y.; Zhang, L.; Deng, J.; Xia, Y.; Zhao, Z.; Meng, X.; Liu, Y. *Inorg. Chem.* **2011**, *50*, 2534−2544.
(10) Jiao, F.; Harrison, A.; Jumas, J.-C.; Chadwick, A. V.; Kockelmann, W.; Bruce, P. G. *J. Am. Chem. Soc.* **2006**, *128*, 5468−5474.
(11) Lee, J.; Orilall, M. C.; Warren, S. C.; Kamperman, M.; DiSalvo, F. J.; Wiesner, U. *Nat. Mater.* **2008**, *7*, 222−228.
(12) Klemm, D.; Kramer, F.; Moritz, S.; Lindström, T.; Ankerfors, M.; Gray, D.; Dorris, A. *Angew. Chem., Int. Ed.* **2011**, *50*, 5438−5466.
(13) Ranby, B. G. *Acta Chem. Scand.* **1949**, *3*, 649−650.
(14) Beck-Candanedo, S.; Roman, M.; Gray, D. G. *Biomacromolecules* **2005**, *6*, 1048−1054.
(15) Kelly, J. A.; Giese, M.; Shopsowitz, K. E.; Hamad, W. Y.; MacLachlan, M. J. *Acc. Chem. Res.* **2014**, *47*, 1088−1096.
(16) Liu, S.; Luo, X.; Zhou, J. *Magnetic Responsive Cellulose Nanocomposites and Their Applications*; InTech: Rijeka, Croatia, 2013.
(17) Ma, M.-G.; Zhu, J.-F.; Li, S.-M.; Jia, N.; Sun, R.-C. *Mater. Sci. Eng., C* **2012**, *32*, 1511−1517.
(18) Zhou, J.; Li, R.; Liu, S.; Li, Q.; Zhang, L.; Zhang, L.; Guan, J. *J. Appl. Polym. Sci.* **2009**, *111*, 2477−2484.
(19) Xiong, R.; Lu, C.; Wang, Y.; Zhou, Z.; Zhang, X. *J. Mater. Chem. A* **2013**, *1*, 14910−14918.
(20) Mahmoud, K. A.; Lam, E.; Hrapovic, S.; Luong, J. H. T. *ACS Appl. Mater. Interfaces* **2013**, *5*, 4978−4985.
(21) Yu, X.; Tong, S.; Ge, M.; Zuo, J.; Cao, C.; Song, W. *J. Mater. Chem. A* **2013**, *1*, 959−565.
(22) Liu, S.; Tao, D.; Zhang, L. *Powder Technol.* **2012**, *217*, 502−509.
(23) Rafi, M. M.; Ahmed, K. S.; Nazeer, K. P.; Siva Kumar, D.; Thamilselvan, M. *Appl. Nanosci.* **2014**, 1−6.
(24) Wu, Y.; Zhu, P.; Reddy, M. V.; Chowdari, B. V. R.; Ramakrishna, S. *ACS Appl. Mater. Interfaces* **2014**, *6*, 1951−1958.
(25) Fei, X.; Shao, Z.; Chen, X. *J. Mater. Chem. B* **2013**, *1*, 213−220.
(26) Sreeram, K. J.; Nidhin, M.; Nair, B. U. *Colloids Surf. B* **2009**, *71*, 260−267.
(27) Singh, J.; Srivastava, M.; Dutta, J.; Dutta, P. K. *Int. J. Biol. Macromol.* **2011**, *48*, 170−176.
(28) Chang, M.-Y.; Wang, W.-H.; Chung, Y.-C. *J. Mater. Chem.* **2011**, *21*, 4966−4970.
(29) Tang, H.; Zhou, W.; Lu, A.; Zhang, L. *J. Mater. Sci.* **2014**, *49*, 123−133.
(30) Klem, M. T.; Young, M.; Douglas, T. *J. Mater. Chem.* **2010**, *20*, 65−67.
(31) Zhou, W.; He, W.; Ma, J.; Wang, M.; Zhang, X.; Yan, S.; Tian, X.; Sun, X.; Han, X. *Mater. Sci. Eng., C* **2009**, *29*, 1893−1896.
(32) Peng, W.; Zhu, S.; Wang, W.; Zhang, W.; Gu, J.; Hu, X.; Zhang, D.; Chen, Z. *Adv. Funct. Mater.* **2012**, *22*, 2072−2080.
(33) Liu, S.; Zhang, L.; Zhou, J.; Xiang, J.; Sun, J.; Guan, J. *Chem. Mater.* **2008**, *20*, 3623−3628.
(34) Ding, J.; Fan, T.; Zhang, D.; Saito, K.; Guo, Q. *Solid State Commun.* **2011**, *151*, 802−805.
(35) Sadakane, M.; Kato, R.; Murayama, T.; Ueda, W. *Mater. Lett.* **2012**, *81*, 80−83.
(36) Ivanova, A.; Fattakhova-Rohlfing, D.; Kayaalp, B. E.; Rathouský, J.; Bein, T. *J. Am. Chem. Soc.* **2014**, *136*, 5930−5937.
(37) Camarero Espinosa, S.; Kuhnt, T.; Foster, E. J.; Weder, C. *Biomacromolecules* **2013**, *14*, 1223−1230.
(38) Wang, N.; Ding, E.; Cheng, R. *Polymer* **2007**, *48*, 3486−3493.
(39) Swanson, H. E. *Standard X-ray diffraction powder patterns*; U.S. Department of Commerce, National Bureau of Standards, U.S. G.P.O.: Washington, DC, 1953.
(40) Musić, S.; Krehula, S.; Popović, S. *Mater. Lett.* **2004**, *58*, 2640−2649.
(41) Chaudhari, N. K.; Yu, J.-S. *J. Phys. Chem. C* **2008**, *112*, 19957−19962.
(42) Wang, W.; Howe, J. Y.; Gu, B. *J. Phys. Chem. C* **2008**, *112*, 9203−9208.
(43) Xavier, A. M.; Ferreira, F. F.; Souza, F. L. *RSC Adv.* **2014**, *4*, 17753−17759.
(44) McIntyre, N. S.; Zetaruk, D. G. *Anal. Chem.* **1977**, *49*, 1521−1529.
(45) Johansson, L.-S.; Campbell, J. M. *Surf. Interface Anal.* **2004**, *36*, 1018−1022.
(46) Aulin, C.; Ahola, S.; Josefsson, P.; Nishino, T.; Hirose, Y.; Österberg, M.; Wågberg, L. *Langmuir* **2009**, *25*, 7675−685.
(47) Cui, X.; Liu, T.; Zhang, Z.; Wang, L.; Zuo, S.; Zhu, W. *Powder Technol.* **2014**, *266*, 113−119.
(48) Dong, X. M.; Kimura, T.; Revol, J.-F.; Gray, D. G. *Langmuir* **1996**, *12*, 2076−2082.
(49) Doniach, S.; Sunjic, M. *J. Phys. C* **1970**, *3*, 285−291.

DOI: 10.1021/ic502446f
Inorg. Chem. 2015, 54, 1129−1135